Resolving the location of small intracontinental earthquakes using Open Access seismic and geodetic data: lessons from the 18 January 2017 m_b 4.3 Ténéré, Niger, earthquake

Timothy J. Craig
COMET, School of Earth and Environment, The University of Leeds,
Leeds, United Kingdom. LS2 9JT
Corresponding author: t.j.craig@leeds.ac.uk

Steven J. Gibbons
NGI, Sognsveien 72, N-0855 Oslo, Norway

This submission is a non-peer reviewed preprint, available via EarthArXiv

Resolving the location of small intracontinental earthquakes using Open Access seismic and geodetic data: lessons from the 18 January 2017 m_b 4.3, Niger, earthquake

Timothy J. Craig
COMET, School of Earth and Environment, The University of Leeds, Leeds, United Kingdom. LS2 9JT
t.j.craig@leeds.ac.uk

Steven J. Gibbons
NGI, Sognsveien 72, N-0855 Oslo, Norway

April 29, 2022

Abstract

A low-magnitude earthquake was recorded on January 18, 2017, in the Ténéré desert in northern Niger. This intraplate region is exceptionally sparsely covered with seismic stations and the closest open seismic station, G.TAM in Algeria at a distance of approximately 600 km, was unusually and unfortunately not operational at the time of the event. Body-wave magnitude estimates range from m_b4.2 to m_b4.7 and both seismic location and magnitude constraints are dominated by stations at teleseismic distances. The seismic constraints are strengthened considerably by array stations of the International Monitoring System for verifying compliance with the Comprehensive Nuclear Test-Ban-Treaty. This event, with magnitude relevant to low-yield nuclear tests, provides a valuable validation of the detection and location procedure for small land-based seismic disturbances at significant distances. For seismologists not in the CTBT system, the event is problematic as data from many of the key stations are not openly available. We examine the uncertainty in published routinely-determined epicenters by performing multiple Bayesloc location estimates with published arrival times considering both all published arrival times and those from open stations only. This location exercise confirms lateral uncertainties in seismologically-derived location no smaller than 10 km. Coherence for InSAR in this region is exceptionally high, and allows us to confidently detect a displacement of the order 6 mm in the time-frame containing the earthquake, consistent with the seismic location estimates, and with a lateral length scale consistent with an earthquake of this size, allowing location constraint to within one rupture length (≤ 5 km) – significantly reducing the lateral uncertainty compared with relying on seismological data only. Combining Open Access-only seismological and geodetic data, we precisely constrain the source location, and conclude that this earthquake likely had a shallow source. We then discuss potential ways to continue the integration of geodetic data in the calibration of seismological earthquake location.

Keywords: Earthquake source observations, Seismicity and tectonics, Satellite geodesy, Earthquake hazards, Earthquake monitoring and test-ban treaty verification

1 Introduction

On the 18^{th} January, 2017, a small-magnitude earthquake occurred in the Ténéré desert of northern Niger (Figure 1a). Located at the northern edge of the Sahel, bordering the Sahara, and roughly half way between the coasts of West Africa and the Red Sea, the source region is deep in the interior of Africa, far from any major population centres – the nearest city being Agadez, $\sim$400 km away. The region is similarly remote from a tectonic perspective - the nearest active plate boundaries are in northern Morocco ($\sim$ 2000 km), the Gulf of Suez ($\sim$ 2400 km) and the East Africa Rift System ($\geq$ 3000 km). The nearest instrumentally-recorded earthquake to the 2017 event, of any magnitude, in the combined catalogues of Bulletin of the International Seismological Centre (ISC Bulletin hereafter; ISC (2021)), is a similarly-remote m_b4.5 earthquake in the southern Ahaggar mountains of Algeria, $\sim$600 km away. Within 15 degrees ($\sim$1650 km) of the Ténéré earthquake, there are only 625 earthquakes reported in the full ISC Bulletin, of any magnitude.

As a result of the tectonic quiescence and remoteness of the region, Ténéré is one of the least-well seismologically instrumented continental regions on Earth, with the nearest seismic station located over 600 km away (at Tamanrasset, southern Algeria - which was in fact inoperative at the time of this earthquake), and no other stations within 1000 km. For small-magnitude earthquakes, data from seismic networks at local and regional distances is crucial for the robust and accurate determination of the earthquake location (e.g. Bondár et al, 2004). In the absence of such data, the 2017 Ténéré earthquake offers an opportunity to test the resolving power of global seismic networks, and the limitations of seismological location routines in the absence of near-field data. With the lack of vegetation, and the lack of major agricultural or industrial activity in the area, the Ténéré desert is also a region where the coherence of interferometric synthetic aperture radar (InSAR) images is high, enabling the detection of small-magnitude surface displacements, and we thus also aim to test how satellite geodesy can complement seismological approaches in the location of small earthquakes in remote continental areas.

Routine seismological catalogues determined the location ($\sim 19.6°N, 10.6°E$), and magnitude ($m_b 4.2 - 4.7$) of this earthquake (see Table 1). The reported magnitude of this earthquake places it in the range of interest for low-yield nuclear tests (e.g. Barker et al, 1998; Chun et al, 2011). For such events, routine seismological monitoring is supplemented by the observational capabilities of the International Monitoring System (IMS), under the auspices of the Comprehensive Test Ban Treaty Organisation (CTBTO), most particularly through a global network of small-aperture seismic arrays and high-quality three-component seismometers. However, data from many of these networks remain subject to access restrictions, and are not currently freely available to the scientific community. This study probes how far events like the Ténéré earthquake can be studied and characterised in detail using only freely-available Open Access data, and tests how reliant the location of such earthquakes is on closed-access data. We combine remote seismological and geodetic analysis to assess the validity with which routine processing approaches were able to determine the location of this earthquake. We highlight a number of issues that may cause problems for the location of rare small earthquakes in remote continental interiors, and demonstrate how the combination of careful seismological analysis with modern geodetic data can mitigate such problems, allowing the high-resolution characterisation of such events.

2 Overview of the Seismological Observations

Figure 1 displays the source region of the January 18, 2017, earthquake together with the locations of events in the ISC GEM catalog (ISC-GEM, 2021) (unrestricted) and the ISC Bulletin (limited to those within 15°), and the locations of seismic stations used to constrain the location in the bulletins listed in Table 1. The map in panel (a) confirms both the absence of significant seismic events in an almost continental-scale region surrounding the epicenter and the sparsity of stations at local, regional, or far-regional distances contributing to the location estimates. Of those stations at far-regional distances (a term usually referring to distances between 10° and 20°) only the three-component station GT.DBIC in the Ivory Coast is open for public access. Panels (b), (c) and (d) of Figure 1 show the signal on GT.DBIC both in a high frequency bandpass (1-4 Hz) and the lower frequency band from 12.5 s to 50.0 s period. The short-period band signals are typical of far-regional continental propagation with high frequency Pn and Sn arrivals followed by high-amplitude and slightly lower period Lg waves which dominate the wavetrain. Both Pn and Sn arrivals are followed by long codas with high-frequency energy. Both body waves and surface waves are visible in the longer period signal although the *Pn* and *Sn* arrivals have low Signal-to-Noise Ratio (SNR). Only the *Pn* arrival is particularly useful for location purposes; the Sn arrival is extremely emergent and picking an accurate signal onset is difficult. In addition, even if the *Pn* arrival-time can be read accurately, the distance-range for this station is associated with an exceptionally large uncertainty in the modelled traveltime (e.g. Myers et al, 2015). The primary value of the DBIC signal is in the estimation of magnitude and the hypothesis that the event is relatively shallow in order to explain the dominant *Lg* and surface waves.

Figure 2 provides both a representative selection of the available teleseismic waveforms and an overview of the global station coverage, again differentiating between stations open to the general public and those limited to authorized parties in the CTBT system. For a seismic event with significant continental landmass in all directions within distances of 100 degrees (i.e. where you would anticipate observing *P*-waves) there is an exceptional degree of asymmetry to the observing seismic network. We have examined significant numbers of open waveforms at stations not included in the ISC bulletin, but where data is openly available (see Figure 1a), and found in very few cases signals which both offered a high SNR and a useful location, covering an azimuthal or distance gap relative to the network displayed in Figure 2. The best signals are found on stations to the North East; in Eastern Europe and Central Asia – a distribution that will be the result of both the network coverage, and the orientation of the focal mechanism and resultant radiation pattern (note that the focal mechanism for this earthquake is unknown). Figure 2 shows signals on the vertical components of three 3-component stations, and (vertical component) array beams on three array stations.

Of the waveforms shown on Figure 2, the Makanchi array (MKAR) is a 9-site primary IMS seismic array in Kazakhstan, the Mount Meron array (MMAI) is a 16-site auxiliary IMS seismic array in Israel, and the Bukovina array (BURAR) is a non-IMS 9-element array in Romania. The data from all of these arrays are openly available; MKAR and BURAR are available via the IRIS Data Management Center and MMAI is available via the GEOFON data center at GFZ Potsdam. Each of these arrays has an aperture of only a few km, with the intention that short period signals (e.g. 1-4 Hz) are coherent between sensors and that the SNR of signal arrivals can be improved by delay-and-stack beamforming (e.g. Rost and Thomas, 2009). Similarly, estimating the coherence or relative power of beams in different directions allows us to estimate the backazimuth and apparent velocity of incoming wavefronts. This assists in algorithms to associate detections and helps to build confidence that a given signal detection is indeed associated with our event hypothesis, on the basis of directional coherence of arrivals.

For each array in Figure 2, the top panel shows the array beam constructed using the predicted backazimuth and *P*-wave slowness, based on the ISC location. Beneath each of the array beams is a scan of backazimuth as a function of time (for a fixed apparent velocity based on the expected earthquake epicentre) and a scan of apparent velocity as a function of time (for a fixed value of the backazimuth based on the expected earthquake epicentre). These plots are a variant on the VESPA process (Davies et al, 1971) and allow us to confirm that each of the signals at the time of the predicted P-arrival is associated with a coherent wave packet with a direction consistent with the origin hypothesis. Gibbons et al (2016) performed such analysis on several array stations for an earthquake of similar magnitude near the Northern tip of Novaya Zemlya in the Russian Arctic and found double bursts of coherent energy with a delay of just over 3 seconds at stations at different azimuths from the epicenter. This observation supported a hypothesis of teleseismic pP phases which helped to constrain the event depth. There is no such unambiguous evidence of depth phases in the array analysis in Figure 2. BURAR and MMAI show very little coherent energy in the coda following the initial arrival; MKAR shows coherent energy with appropriate propagation parameters far into the coda.

The remaining three panels of Figure 2 show signals for the P-arrivals at arbitrarily chosen teleseismic 3-component stations (in Czechia, Saudi Arabia, and Kenya). We note that the SNR for the signals at many of these stations is relatively poor, and that improvement through stack-and-delay is not possible for non-array stations. The waveforms shown in Figure 2 also highlight the potential subjectivity in identifying the onset of a particular phase arrival, with the majority of arrivals being emergent, especially in terms of identifying a confirmed signal above the level of noise. We see no unmistakable depth phases, which would offer a high-precision constraint on the event depth. A few stations show multiple bursts of energy but there is insufficient evidence at any station to label with confidence the later arrivals as depth phases.

Summarising the available seismological data, we are left with a comparatively sparse set of phase observations, of variable, but often limited, precision. The advantages in signal identification and arrival precision that arise from the enhanced processing of small aperture arrays is clear. But only a few of the operators of these stations make their waveform data Open Access (see Figure 2). Similarly, many of the more isolated three-component stations, vital for filling gaps in azimuthal and epicentral coverage, remain closed to the general public. Combined, these pose the question of how reliant high-precision earthquake location is on closed-access data, and how well characterised events such as the Ténéré earthquake can be, using only Open Access seismic data.

3 Seismic Location Estimates for the 18 January 2017 Niger Earthquake

Figure 3 shows the epicenters listed in Table 1 together with their published 95% confidence ellipses. The epicenters reported by the NEIC/USGS (National Earthquake Information Center/United States Geological Survey) and CTBTO/IDC (Comprehensive Nuclear Test-Ban-Treaty Organization/International Data Center) lie comfortably within the confidence ellipse reported by the other agency, and there is significant overlap between the two confidence ellipses. The epicenter reported by the International Seismological Center (ISC, 2021) lies within both of these confidence ellipses but is itself associated with a much smaller confidence ellipse which does include the CTBT epicenter estimate, but not the NEIC epicenter estimate. A fourth location estimate is provided in the ISC catalog summary: the ISC-EHB estimate (ISC-EHB, 2021), named after Engdahl, van der Hilst, and Buland. This epicenter lies to the southeast and outside of all of the other 95% confidence ellipses. The ISC-EHB estimate itself is associated with a far smaller confidence ellipse which overlaps little with the other 95% confidence ellipses. All of these confidence ellipses share a similar azimuth of the semi-major axis: all around 120°. This is easy to understand in terms of the station distribution (c.f. Figure 2) since the density of contributing stations in directions from North to East (i.e. in Europe and Central Asia) is substantially greater than in other directions. The final location estimate is that from the European Mediterranean Seismological Center (EMSC, e.g. Godey et al, 2013) and this lies approximately 20 km to the South East of the ISC and CTBT locations. Like the NEIC estimate, the EMSC solution is published fairly rapidly and is attributed a relatively large confidence ellipse. However, the EMSC solution is more dominated by stations to the North (Europe) than the NEIC solution which is consistent with the rather different epicenter estimate and orientation of the confidence ellipse. Given the discrepancy between the EMSC solution and the ISC and CTBT locations, we will not be subjecting the EMSC solution to further analysis.

Comparing the various epicenters and corresponding confidence ellipses is difficult since the solutions use varying combinations of arrival-time readings, station distributions, weights, and location algorithms. Only the NEIC, CTBT, and EMSC catalogs are truly independent. Although the solutions have a number of stations in common, the readings are made by different analysts and using different systems and location procedures. The ISC catalog, and the ISC-EHB solution, exploit phase readings from multiple catalogs and can frequently use two or more alternative arrival time estimates, reported by different agencies, for the same phase arrival to constrain an event. TORD in southwestern Niger and KEST in Tunisia are two of the stations in the ISC bulletin that are closest to the earthquake epicenter (see Figure 1). Both stations are primary seismic stations of the International Monitoring System and, to the best of our knowledge, the data from neither are available to users other than those with access authorized by National Data Centers in the CTBT system. The USGS has access to this data via the United States National Data Center and is authorized to use arrival-time estimates from these stations when forming their earthquake bulletin.

The ISC bulletin provides two estimates for the Pn arrival time at TORD: 21:50:53.534

and 21:51:02.71, reported by the IDC and the NEIC respectively. Only the first of these is a defining phase in the ISC catalog, with a time residual of -0.7 seconds. The second is labelled a "Questionable onset" (with a time residual of 8.5 seconds) and does not contribute to the solution. The ISC bulletin also provides two estimates for the Pn arrival time at KEST: 21:52:07.30 and 21:52:06.98, again provided by the IDC and the NEIC respectively. Both of these arrivals (with time-residuals of -0.7 seconds and -1.0 seconds respectively) are defining arrivals in the ISC solution. In the ISC-EHB bulletin, all four of these arrival times are defining phases for the location estimates with time residuals listed as -2.1 seconds (TORD Pn, IDC), 7.1 seconds (TORD Pn, NEIC), -1.4 seconds (KEST Pn, IDC), and -1.7 seconds (KEST Pn, NEIC). The time residual on the TORD Pn arrival is large for both the ISC and ISC-EHB solutions. The size of the time residual led it to be disregarded from the ISC solution. While it is a defining phase in the ISC-EHB solution, it is not easy to estimate the effect it has on the solution without a thorough examination of the weights and the provenance of the location algorithm.

The discrepancy between the ISC-EHB epicenter and the other epicenters is likely a combination of many such differences. The waveforms displayed in Figures 1 and 2 make it clear how emergent and ambiguous some of the phase arrival time estimates may be. Often the highest amplitude comes several seconds after what appears to be the first signal onset and we may have to make judgements regarding what is a likely first P-arrival and what is a possible depth phase. The first part of the signal visible above the background noise may be significantly later than the true onset time if we have an emergent signal or a depth phase with a higher amplitude than the first P-arrival. Without access to the waveform data, it is not possible for an independent seismologist to evaluate the quality of the arrival time estimates, limiting our ability to determine where pick uncertainty may be driving the discrepancies in location estimates. The seismic event location procedures employed at the different agencies are under continual revision and overviews of recent progress at the NEIC and IDC are given by Benz (2017) and Koch (2013) respectively. Details of improvements to the ISC location algorithm can be found in Bondár and Storchak (2011) and references therein. A comprehensive description of the exact procedures employed at a given observatory, so detailed that they could be reproduced exactly by a different observatory, is unrealistic.

However, we can gain more understanding as to how the location estimates depend upon the choice of stations alone by performing new location estimates using a common algorithm with the arrival times used for the different catalogs displayed in Figure 3. We use the Bayesloc program (Myers et al, 2007) which can solve for the locations of multiple seismic events simultaneously by a Monte Carlo Markov Chain (MCMC) procedure to find a joint probability distribution for the events' origins, origin parameter uncertainties, and for empirical corrections to modelled traveltimes. Prior constraints, for example Ground Truth event locations or existing models for traveltime corrections, can be applied if available to improve the quality of the posterior probability distributions. Although the program is designed for, and is most effective with, large clusters of seismicity, it can also be run for a single event. Having only a single event of course precludes, for example, the calculation of empirical traveltime corrections (since we cannot resolve between the contributions to arrival-time anomalies resulting from velocity variations and those resulting from picking errors). For each iteration of the MCMC routine, the program writes out the epicenter coordinates. Over a single run, many thousands of origin hypotheses are written out generating a cloud. The size and shape of this cloud provides a visualization of the uncertainty associated with the location which may show a more complex geometry than the classical formal confidence ellipses. Given the absence of prior constraints, and the fact that we only have a single event, our main motivation for using Bayesloc is this ability to visualize any irregularities in the geometry of the location probability distribution.

Figure 4 displays the clouds of trial epicenter estimates from the Bayesloc calculations for four different combinations of stations. In panel (a) the event is located using only the phase arrival times listed in the USGS/NEIC bulletin. The red symbols are the epicenters output when we only use those stations for which waveform data can be obtained without barrier by an arbitrary user from only open sources (red symbols in panel (b)). The grey symbols are the epicenters output when we also allow use of the arrival times from stations for which waveform data are not available without specific authorization (white symbols in panel (b)). We attempt to better visualize the spread of the point clouds by plotting the 90, 95, and 99% confidence ellipses based upon the statistics of the coordinates, although we stress that the point cloud distributions may display significant departures from the geometries indicated by the ellipses. The inclusion of the closed access stations reduces the apparent spread somewhat although the difference is not large. As noted earlier, the TORD arrival in this dataset is associated with a large time-residual and so it may have had very little influence on the solutions. We note also that the Bayesloc epicenter clouds using the USGS/NEIC arrival estimates are consistent with the bulletin epicenter estimate.

Panel (c) of Figure 4 shows the corresponding Bayesloc epicenter clouds for the arrivals listed in the ISC bulletin, with the corresponding station maps displayed in panel (d). There is a significant difference between the spread of the epicenter clouds for the "complete" and "strictly open" station networks for the ISC arrivals. We note that not only is the TORD time-residual far smaller for one of the arrivals in the ISC solution, but there are 3 other network stations, KIC, TIC, and LIC which add extra constraints from the South West. These stations are all very close to DBIC, in the Ivory Coast, and they do not much increase the azimuthal coverage. However, their inclusion may change the weight of the constraints from that direction considerably. We note in addition, an extra constraint from the Soneca Array (ESDC) in Spain from the CTBT bulletin. This is in a direction in which there are no open stations with good signals or clear picks. This may be an example of where the use of beamforming of signals on a seismic array may make a usable phase arrival where one was not sufficiently strong on a single channel, allowing the identification of arrivals even in regions where the radiation pattern leads to comparatively low amplitudes. The Bayesloc epicenter clouds lie a few km to the South East of the ISC bulletin epicenter, and to the West of the epicenter provided in the ISC-EHB bulletin. The differences in the location estimates are likely due to both different weightings of the phase arrivals and differences in the location algorithms.

To summarize, with the available seismic stations, there is a lateral uncertainty of at least 10 km in the epicentral estimates. The epicenter from the ISC-EHB bulletin appears to be an outlier and, given the set of arrivals from which this solution is formed, the quoted 95% confidence interval would appear to be optimistic. We can move the epicenter estimate by several km by changing the observing network alone, but never by more than around 10 km. Had the seismic signals from this event had characteristics of an explosion, the confidence region from the seismic signals is sufficient for the criteria for a permissible On-Site-Inspection following Entry Into Force of the Comprehensive Nuclear Test-Ban-Treaty. The treaty text states "The area of an on-site inspection shall be continuous and its size shall not exceed 1,000 square kilometres. There shall be no linear distance greater than 50 kilometres in any direction" (UN, 1998). Even with the existing network (and there are no non-IMS stations in the bulletins considered here at any significantly closer distances or covering any significant azimuthal gaps), Figure 4 indicates that the location uncertainty is well within these limits. The completed IMS, as listed in the treaty text, contains in addition stations not currently operating that would likely have improved the constraints on this event (in particular, the Luxor array in Egypt: 26.0 °N 33.0 °E, not yet constructed, and the BGCA 3-component station in the Central African Republic: 5.176 °N, 18.424 °E, installed but not currently operational). Another IMS 3-component station, KOWA, in Mali, is now operational but was not at the time of this earthquake (Data from IU.KOWA is openly available to the community via IRIS). There are few opportunities for further reducing the uncertainty in the seismic location estimates without additional, closer, stations. For example, there are no nearby seismic events from which we could perform a calibrated or relative location estimate (e.g. Douglas, 1967, and subsequent studies of joint epicentral determination and multiple event location). The scarcity of seismic observations in the region also means that regional 3D seismic velocity models remain unrefined and uncalibrated.

4 Surface displacement from the 18 January 2017 Niger Earthquake using InSAR Data

In the case of remote continental earthquakes, with a sparsity of near-field seismological data, the recently-developed global coverage of satellite radar offers an additional dataset to which may help constrain earthquake locations, and complement those constraints available from seismology. The limiting factor in locating an earthquake using satellite geodesy is not directly the magnitude of the earthquake, but instead the amplitude of the surface deformation, and whether any signal can be detected. Whilst the Ténéré earthquake is lower magnitude than typically studied using InSAR (e.g., Weston et al, 2012; Funning and Garcia, 2019), other small-magnitude events have been detected in the past (Lohman and Simons, 2005; Ritz et al, 2020), in cases where the earthquake is very shallow, allowing higher-amplitude near-fault displacements to be expressed at the surface. Whereas converting remote seismological observations to an source location can be subject to major uncertainties on the scale of 10's of kilometres, particularly relating the velocity structure, geodetic measurements offer the direct detection of near-fault displacement, in the ideal case where a fault breaks the surface, can determine the fault location with pixel-scale resolution (typically 10's of metres). Therefore, whilst InSAR offers no constraint on the earthquake origin time, places no constraints on the rupture evolution, and, for small-magnitude events, can only detect shallow sources (Mellors et al, 2004), it can offer a valuable complement to seismological observations, placing precise constraints on the location of the rupture plane.

To supplement the available seismic data, we process interferometric synthetic aperture radar (InSAR) images for the source region using data from the European Space Agency's Sentinel-1 satellites. We use acquisitions that span the earthquake date, and construct interferograms using all potential pairs where the earthquake occurs within a timespan of up to four consecutive acquisitions (Figure 5). Processing was carried out using the LiCSAR system (Lazecký et al, 2020, to which readers are directed for a full description of the processing approach). Each interferogram is processed using multilooking factors of 5 in range and 20 in azimuth, with interferograms therefore having a spatial resolution of $\sim 100 \times 100$ m per pixel. Data are then subject to spatial filtering using an adaptive power spectrum filter. Due to the remote location, only ascending track data were being routinely acquired at the time of our study earthquake, with a 12-day repeat time. Coherence in the region at such short temporal baselines is good – the region is unvegetated desert, and whilst migratory sand can cause problems for radar interferometry, this does not appear to be the case around our earthquake, although we note that the dune fields to the south and southwest show markedly lower coherence. In Supplementary Material, Figure S2 shows average coherence prior to spatial filtering at 12, 24 and 36 day temporal baselines across the whole Sentinel-1 archive. As demonstrated by

Figure 5 and Figure 6, after spatial filtering, coherence at the wavelengths of interest for earthquake-related processes is extremely high. Given the lack of major topographic features, there is minimal topographically-correlated atmospheric noise, although all interferograms are subject to long-wavelength noise presumed to result from a combination of atmospheric variations and orbital effects (see Figures 5 and 6). One SAR acquisition (20161216) features NE-SW orientated bands which are clearly unrelated to either the regional tectonics or our study earthquake. Although the exact origin of these features is uncertain, they are most likely to be atmospheric rolls. Some of the interferograms shown in Figure 6, which do not span the earthquake, show significantly higher levels of noise, which we presume to be atmospheric in origin, showing that even here, atmospheric variability can strongly influence the detection of tectonic signals, although it does not hinder our observations of the 2017 Ténéré earthquake.

All coseismic interferograms feature a small, roughly circular, displacement signal at $\sim 19.6°$ N, 10.6°E, highlighted by the black circle on Figure 5. This signal displays a spatial pattern as expected for a small-magnitude earthquake, is at a wavelength where we would expect the deformation signal from a m_b4.3 to be (1 – 5 km, based on a rupture length of ≤ 1 km following the established earthquake scaling relationships; Wells and Coppersmith, 1994), is common to all interferograms that span the earthquake date, and is not present in any interferograms that do not span the earthquake (see Figure 6 for examples). We are therefore confident that this signal relates to our study earthquake, despite the small amplitude of the observed signal.

To improve the resolution of this signal, we construct a simple linear stack of 3 fully independent interferograms (20161204-20170202, 20161228-20170226, and 20170109-20170310 from Figure 5 – stack shown in Figure 7a). To remove long-wavelength atmospheric effects, and to isolate signals at wavelengths likely to be related to a m_b4.3 earthquake, we spatially filter the InSAR data using a 4-pole Butterworth filter, bandpassed between 15000 and 500 metres (Figure 7b).

The resulting stack shows a clear, coherent line-of-sight displacement of up to 6 mm. Only one lobe of the deformation field is clearly visible, and although there are indications on the filtered stack of opposite-polarity displacement lobes to the northeast and southeast of the main deformation lobe, these are insufficiently clear to permit the determination of a focal mechanism. We visually assess that the causative fault plane most likely lies to the southeast or northeast of the peak in displacement. The lack of a clear four-lobe pattern of deformation argues against a pure strike-slip mechanism, and we infer that the earthquake therefore involved either dip- or oblique-slip faulting.

The deformation pattern shows no clear discontinuities in phase, either on the stack or on individual interferograms, suggesting that the rupture did not break the surface, and that the top of the fault rupture patch is buried. That there is an observable signal at all, however, from such a small-magnitude event, indicates that the earthquake must have been shallow ($\leq$ 5 km; see Mellors et al (2004); Dawson and Tregoning (2007)), consistent with the lack of any clearly separated depth phases in the seismic data (see Figure 2). In the case of this earthquake, located in the sandy Ténéré desert, we consider it likely that the earthquake ruptured to the top of the consolidated bedrock, but that the deformation signal is subsequently blanketed by overlying less consolidated sandstones, less able to sustain coseismic rupture.

5 Conclusions and Discussion

Figure 7 shows both seismological and geodetic constraints on the location of the 2017 Ténéré earthquake. Of the four catalogue locations published by seismological agencies only those from the CTBT and the initial ISC catalogue are consistent with the more precise location information offered by the InSAR displacement pattern. The location from the NEIC lies marginally too far east, but within its own uncertainty envelope of the geodetic location, whilst the ISC-EHB location lies $\sim$ 15 km to the east-southeast of the geodetic location, substantially beyond its quoted uncertainty interval from the geodetically-observed displacement signal (Figure 3). The EMSC location lies $\sim$ 30 km to the southeast of the detected surface deformation – the furthest of any of the catalogue locations we consider.

Such differences between seismological and geodetic locations are commonly, and widely observed for larger earthquakes (e.g. Weston et al, 2012). However, comparison of geodetic and seismological location is not simple – the two approaches are measuring slightly different aspects of the earthquake. Seismological locations like those applied to this earthquake give a hypocentre – the point of rupture initiation. In contrast, geodetic data like that used here has no capacity to constrain the earthquake initiation, or its rupture process, in time, as the displacement seen in the interferograms is the result of the complete earthquake rupture. In this case, we are unable to solve robustly for a causative fault plane from the InSAR data, but even if we could, the earthquake hypocentre could still lie anywhere on that rupture plane. For larger earthquakes, with rupture lengths of $>$ 5 km, this can pose additional location problems. However, for a small-magnitude event like the 2017 Ténéré earthquake, where the rupture length is likely to be $<$ 5 km, this discrepancy between the seismological hypocentre and the geodetic fault rupture will be small, compared to the uncertainties in seismological location.

Seismological locations are subject to uncertainty in the solid-Earth velocity structure along the full ray path from source to receiver. In the case of the locations shown in Figure 3 and 4, the relative travel-time difference between all the locations shown is $<$ 0.5 s for regional arrivals and $<$ 0.2 s for teleseismic arrivals. As demonstrated in Figure 2, the majority of arrivals are emergent, and picking a precise onset is usually subject to uncertainties on at least this magnitude. This is then compounded by the variation in predicted travel times between different velocity models. Many location routines use a standard global 1-dimensional velocity structure. Inclusion of the 3D Earth structure, whilst possible (e.g. Simmons et al, 2021, and references therein), remains subject to relatively large uncertainties in areas like Saharan Africa, where coverage from both sources and stations is very poor. In this region, the variation in predicted travel times between simple 1D and more complex 3D velocity models can add an additional 0.5s in travel time uncertainty, equating to a spatial difference on the order of 10 – 20 km. In contrast, locations based on geodetic data are subject to uncertainty derived only from the very-near source elastic structure. For shallow earthquakes, in particular, the impact that this has on geodetic earthquake location is minimal.

Seismological estimates for the magnitude of the Ténéré earthquake vary between m_b 4.2 (IDC) and m_b 4.7 (EMSC). Although without formally determining the amount of slip, we are unable to use the InSAR data to quantitatively estimate a comparable geodetic magnitude, we note that that surface displacement wavelength of the deformation imaged using InSAR is perhaps longer than would be expected, particularly at the lower end of the range of m_b estimates. As the InSAR deformation field captures all deformation between the two acquisition dates, we cannot rule out the possibility that the displacement seen is enhanced by some level of aseismic process. However, this would be rare for an earthquake of this magnitude.

The consideration of both InSAR and seismological data for small magnitude earthquakes, as shown here, therefore demonstrates the potential for geodetic data to both supplement, and potentially calibrate, seismological earthquake location, allowed the determination of high-precision absolute spatial locations for small earthquakes with small rupture lengths. Such characterisation has several potential applications. Firstly, such high precision location constraints have the potential to contribute to the monitoring and discrimination capabilities of the CTBT, particularly in remote areas, far from near-field seismological instrumentation. Secondly, high-precision geodetic earthquake locations can be used to calibrate regional seismological locations, which are often subject to large systematic uncertainties due to biases in velocity structure and in network geometry. Thirdly, in cases where accurate arrival times can be determined, precise locations allow the use of small earthquakes in remote places to be used for the validation of tomographic models for the solid-Earth velocity structure, supplementing sparse available equivalents from controlled-source seismic signals (usually explosions: Bondár and McLaughlin, 2009).

Our study on the 2017 Ténéré therefore illustrates the potential for satellite radar to supplement the monitoring capabilities of traditional seismological networks for earthquake location, particularly in remote areas, and particularly in areas with high coherence. As the footprint of satellite missions, and the coverage of routine processing, expands, the potential for InSAR to be brought in to routine earthquake monitoring will only increase. Seismic detectability maps have long been employed to estimate thresholds for the magnitudes of seismic disturbances which can confidently be detected and location in a given region for a given monitoring network (e.g. Kværna and Ringdal, 2013). Going forwards, we would recommend developing from the theoretical work of Mellors et al (2004); Dawson and Tregoning (2007), and building towards global detectability maps for geodetic observation, although we recognise that these would need to build in the limitations posed by the tradeoff between depth and magnitude of displacement detectability, and time-variable nature of both decorrelation and non-tectonic (e.g., atmospheric) noise in satellite radar. Funning and Garcia (2019) suggested that there is a magnitude completeness threshold for global earthquake detectability for crustal earthquakes between M_w 6.2 – 7.0 when using Sentinel-1 InSAR data. However, our study, along with a growing number of others (e.g., Ganas et al, 2018; Dalaison et al, 2021; Liu et al, 2021), shows that, whilst far from complete, in certain regions and for particularly shallow earthquakes, there are often detectable signals even for earthquakes down to a $M \sim 4$ which can be used to provide additional constraints on earthquake locations.

The 2017 Ténéré earthquake also illustrates the role that data not routinely available to the academic community play in earthquake location. For both the USGS and the ISC sets of arrivals used in our relocation (see Figure 4), restricting the arrivals used to only Open Access data leads to a marked increase the location uncertainty. Whilst the InSAR data used here, from the European Space Agency's' Sentinel-1 mission, is freely available, the same is not necessarily true for all radar missions. Whilst the radar coherence in the Ténéré is high, allowing up to resolve such small displacements, conducting such work elsewhere, particularly in more vegetated environments, will likely benefit from the use of a range of satellites with different mission parameters, particularly wavelength, and may lead to a similar disparity between Open Access and restricted data that we see in the seismological datasets.

Acknowledgements

TJC was supported in this work by the Royal Society under URF\R1\180088. TJC was also supported through COMET, the UK Natural Environment Research Council's Centre for the Observation and Modelling of Earthquakes, Volcanoes, and Tectonics. We thank Milan Lazecky for his assistance with processing the InSAR data, and Tim Wright for useful discussions. We thank Manon Dalaison and one anonymous reviewer for their comments, which have helped improve this manuscript.

All maps in this paper are created using GMT software (Wessel et al, 2019). Seismograms in Figure 1 and 2 were plotted using Obspy (Beyreuther et al, 2010).

Data Availability

The published location estimates were obtained from the bulletin of the International Seismological Center (ISC, 2021) `http://www.isc.ac.uk/cgi-bin/web-db-v4?event_id=619603285` (ISC, last accessed February 2022) and from the European Mediterranean Seismological Centre `https://www.emsc-csem.org/Earthquake/earthquake.php?id=561096` (EMSC, last accessed February 2022). The USGS/NEIC solution with phase arrival times are published on `https://earthquake.usgs.gov/earthquakes/eventpage/us10007u0v/executive` (United States Geological Survey, last accessed February 2022). The bayesloc program is obtained from `https://www-gs.llnl.gov/nuclear-threat-reduction/nuclear-explosion-monitoring/bayesloc` (last accessed February 2022). InSAR data we retrieved from `https://comet.nerc.ac.uk/comet-lics-portal/` (last accessed February 2022). LiCSAR data contain modified Copernicus Sentinel data [2017] analysed by the Centre for the Observation and Modelling of Earthquakes, Volcanoes and Tectonics (COMET). LiCSAR uses JASMIN, the UK's collaborative data analysis environment (http://jasmin.ac.uk)"

Seismic waveform data was obtained from the following networks of the International Federation of Digital Seismograph Networks (FDSN): BR, CA, CN, CQ, G, GE, GO, GR, GT, HL, HP, HT, II, IS, IU, KO, KR, KZ, MN, NR, RO, TJ, US, XW. We gratefully acknowledge the operators of all of the networks for providing open access to the data and to the Incorporated Research Institutions for Seismology (IRIS, https://www.iris.edu/hq/) and the various nodes of the European Integrated Data Archive (EIDA, https://www.orfeus-eu.org/data/eida/nodes/) for providing access to this data.

References

Barker B, Clark M, Davis P, Fisk M, Hedlin M, Israelsson H, Khalturin V, Kim WY, McLaughlin K, Meade C, North R, Orcutt J, Powell C, Richards PG, Stead R, Stevens J, Vernon F, Murphy J, Wallace T (1998) Monitoring Nuclear Tests. Science 281(5385):1967–1968, DOI 10.1126/science.281.5385.1967, URL `http://dx.doi.org/10.1126/science.281.5385.1967`

Benz H (2017) Building a National Seismic Monitoring Center: NEIC from 2000 to the Present. Seismological Research Letters 88(2B):457–461, DOI 10.1785/0220170034, URL `https://pubs.geoscienceworld.org/srl/article/88/2B/457-461/282939`

Beyreuther M, Barsch R, Krischer L, Megies T, Behr Y, Wassermann J (2010) ObsPy: A Python Toolbox for Seismology. Seismological Research Letters 81:530–533, DOI 10.1785/gssrl.81.3.530

Blandford R (1974) An automatic event detector at the Tonto Forest Seismic Observatory. Geophysics 39(5):633–643, DOI 10.1190/1.1440453, URL http://dx.doi.org/10.1190/1.1440453

Bondár I, McLaughlin K (2009) A New Ground Truth Data Set For Seismic Studies. Seismological Research Letters 80, DOI 10.1785/gssrl.80.3.465

Bondár I, Storchak D (2011) Improved location procedures at the International Seismological Centre. Geophysical Journal International 186(3):1220–1244, DOI 10.1111/j.1365-246x.2011.05107.x, URL http://dx.doi.org/10.1111/j.1365-246x.2011.05107.x

Bondár I, Myers SC, Engdahl ER, Bergman EA (2004) Epicentre accuracy based on seismic network criteria. Geophysical Journal International 156(3):483–496, DOI 10.1111/j.1365-246x.2004.02070.x, URL http://dx.doi.org/10.1111/j.1365-246x.2004.02070.x

Chun KY, Wu Y, Henderson GA (2011) Magnitude Estimation and Source Discrimination: A Close Look at the 2006 and 2009 North Korean Underground Nuclear Explosions. Bulletin of the Seismological Society of America 101(3):1315–1329, DOI 10.1785/0120100202, URL http://dx.doi.org/10.1785/0120100202

Dalaison M, Jolivet R, van Rijsingen E, Michel S (2021) The Interplay Between Seismic and Aseismic Slip Along the Chaman Fault Illuminated by InSAR. Journal of Geophysical Research 126, DOI 10.1029/2021JB021935

Davies D, Kelly DJ, Filson JR (1971) The VESPA process for the analysis of seismic signals. Nature 232:8–13

Dawson J, Tregoning P (2007) Uncertainty analysis of earthquake source parameters determined from InSAR: A simulation study. Journal of Geophysical Research 112, DOI 10.1029/2007JB005209

Douglas A (1967) Joint Epicentre Determination. Nature 215(5096):47–48, DOI 10.1038/215047a0, URL http://dx.doi.org/10.1038/215047a0

Funning G, Garcia A (2019) A systematic study of earthquake detectability using Sentinel-1 Interferometric Wide-Swath data. Geophysical Journal International 216, DOI 10.1093/gji/ggy426

Ganas A, Kourkouli P, Briole P, Moshou A, Elias P, Parcharidis I (2018) Coseismic Displacements from Moderate-Size Earthquakes Mapped by Sentinel-1 Differential Interferometry: The Case of February 2017 Gulpinar Earthquake Sequence (Biga Peninsula, Turkey). Remote Sensing 10, DOI 10.3390/rs10071089

Gibbons SJ, Antonovskaya G, Asming V, Konechnaya YV, Kremenetskaya E, Kværna T, Schweitzer J, Vaganova NV (2016) The 11 October 2010 Novaya Zemlya Earthquake: Implications for Velocity Models and Regional Event Location. Bulletin of the Seismological Society of America 106(4):1470–1481, DOI 10.1785/0120150302, URL http://dx.doi.org/10.1785/0120150302

Godey S, Bossu R, Guilbert J (2013) Improving the Mediterranean seismicity picture thanks to international collaborations. Physics and Chemistry of the Earth, Parts A/B/C 63:3–11, DOI 10.1016/j.pce.2013.04.012, URL https://linkinghub.elsevier.com/retrieve/pii/S1474706513000387

ISC (2021) International Seismological Centre on-line Bulletin. https://doi.org/10.31905/D808B830, DOI 10.31905/D808B830

ISC-EHB (2021) International Seismological Centre ISC-EHB dataset. https://doi.org/10.31905/PY08W6S3, DOI 10.31905/PY08W6S3

ISC-GEM (2021) International Seismological Centre ISC GEM earthquake catalog. https://doi.org/10.31905/d808b825, DOI 10.31905/d808b825

Koch K (2013) Eight Years of Continuous Quality Assessment of the International Data Centre (IDC) Reviewed Event Bulletin. Bulletin of the Seismological Society of America 103(1):296–305, DOI 10.1785/0120110350, URL https://pubs.geoscienceworld.org/bssa/article/103/1/296-305/331565

Kværna T, Ringdal F (2013) Detection Capability of the Seismic Network of the International Monitoring System for the Comprehensive Nuclear Test-Ban-Treaty. Bulletin of the Seismological Society of America 103(2A):759–772, DOI 10.1785/0120120248, URL http://dx.doi.org/10.1785/0120120248

Lazecký M, Spaans K, González P, Maghsoudi Y, Morishita Y, Albino F, Elliott J, Greenall N, Hatton E, Hooper A, Juncu D, McDougall A, Walters RJ, WAtsom C, Weiss J, Wright T (2020) LiCSAR: an Automatic InSAR Tool for Measuring and Monitoring Tectonic and Volcanic Activity. Remote Sensing 12, DOI 10.3390/rs12152430

Liu F, Elliott J, Craig T, Hooper A, Wright T (2021) Improving the Resolving Power of InSAR for Earthquakes Using Time Series: A Case Study in Iran. Geophysical Research Letters 48, DOI 10.1029/2021GL093043

Lohman R, Simons M (2005) Locations of selection small earthquakes in the Zagros mountains. Geochemistry, Geophysics, Geosystems 6, DOI 10.1029/2004GC000849

Mellors RJ, Magistrale H, Earle P, Cogbill A (2004) Comparison of Four Moderate-Size Earthquakes in Southern California Using Seismology and InSAR. Bulletin of the Seismological Society of America 94(6):2004–2014, DOI 10.1785/0120020219, URL https://pubs.geoscienceworld.org/bssa/article/94/6/2004-2014/146971

Myers SC, Johannesson G, Hanley W (2007) A Bayesian hierarchical method for multiple-event seismic location. Geophysical Journal International 171(3):1049–1063, DOI 10.1111/j.1365-246x.2007.03555.x, URL http://dx.doi.org/10.1111/j.1365-246x.2007.03555.x

Myers SC, Simmons NA, Johannesson G, Matzel E (2015) Improved Regional and Teleseismic P-Wave Travel-Time Prediction and Event Location Using a Global 3D Velocity Model. Bulletin of the Seismological Society of America 105(3):1642–1660, DOI 10.1785/0120140272, URL https://pubs.geoscienceworld.org/bssa/article/105/3/1642-1660/332170

Ritz J, Baize S, Ferry M, Larroque C, Audin L, Delouis B, Mathot E (2020) Surface rupture and shallow fault reactivation during the 2019 MW 4.9 Le Teil earthquake, France. Communications Earth and Environment 1, DOI 10.1038/s43247-020-0012-z

Rost S, Thomas C (2009) Improving Seismic Resolution Through Array Processing Techniques. Surveys in Geophysics 30:271–299, URL http://dx.doi.org/10.1007/s10712-009-9070-6, doi:10.1007/s10712-009-9070-6

Simmons NA, Myers SC, Morency C, Chiang A, Knapp DR (2021) SPiRaL: a multiresolution global tomography model of seismic wave speeds and radial anisotropy variations in the crust and mantle. Geophysical Journal International 227:1366–1391, DOI 10.1093/gji/ggab277, URL https://academic.oup.com/gji/article/227/2/1366/6324570

UN (1998) CTBT, Comprehensive Nuclear Test-Ban-Treaty. United Nations, Dept. for Disarmament Affairs and Dept. of Public Information, New York. https://www.ctbto.org/the-treaty/treaty-text/

Wells D, Coppersmith K (1994) New Empirical Relationships among Magnitude, Rupture Length, Rupture Width, Rupture Area, and Surface Displacement. Bulletin of the Seismological Society of America 84:974–2001

Wessel P, Luis JF, Uieda L, Scharroo R, Wobbe F, Smith WHF, Tian D (2019) The Generic Mapping Tools Version 6. Geochemistry, Geophysics, Geosystems 20(11):5556–5564, DOI 10.1029/2019GC008515

Weston J, Ferreira A, Funning G (2012) Systematic comparisons of earthquake source models determined using InSAR and seismic data. Tectonophysics 532-535, DOI 10.1016/j.tecto.2012.02.001

Table 1: Routine catalogue locations for the 2017/01/18 Ténéré earthquake together with 95% confidence ellipses specified with (Smaj/Smin/Az) where Smaj and Smin are the lengths of the major and minor axes in km. ^{f}Depths were fixed *a priori* during location determination.

Catalogue	Origin time (UTC)	Lat (°)	Lon (°)	Dep (km)	(Smaj/Smin/Az)	m_b
IDC	21:48:19.39	19.5947	10.6106	0.0^f	(16.0/12.7/120°)	4.2
ISC	21:48:21.08	19.5847	10.6018	10.0^f	(10.6/7.6/125°)	4.3
NEIC	21:48:22.14	19.6049	10.6491	10.0^f	(16.0/12.7/120°)	4.6
ISC-EHB	21:48:21.08	19.5530	10.7380	10.0^f	(7.1/5.6/117°)	–
EMSC	21:48:21.80	19.48	10.75	10.0^f	(18.5/14.9/93°)	4.7

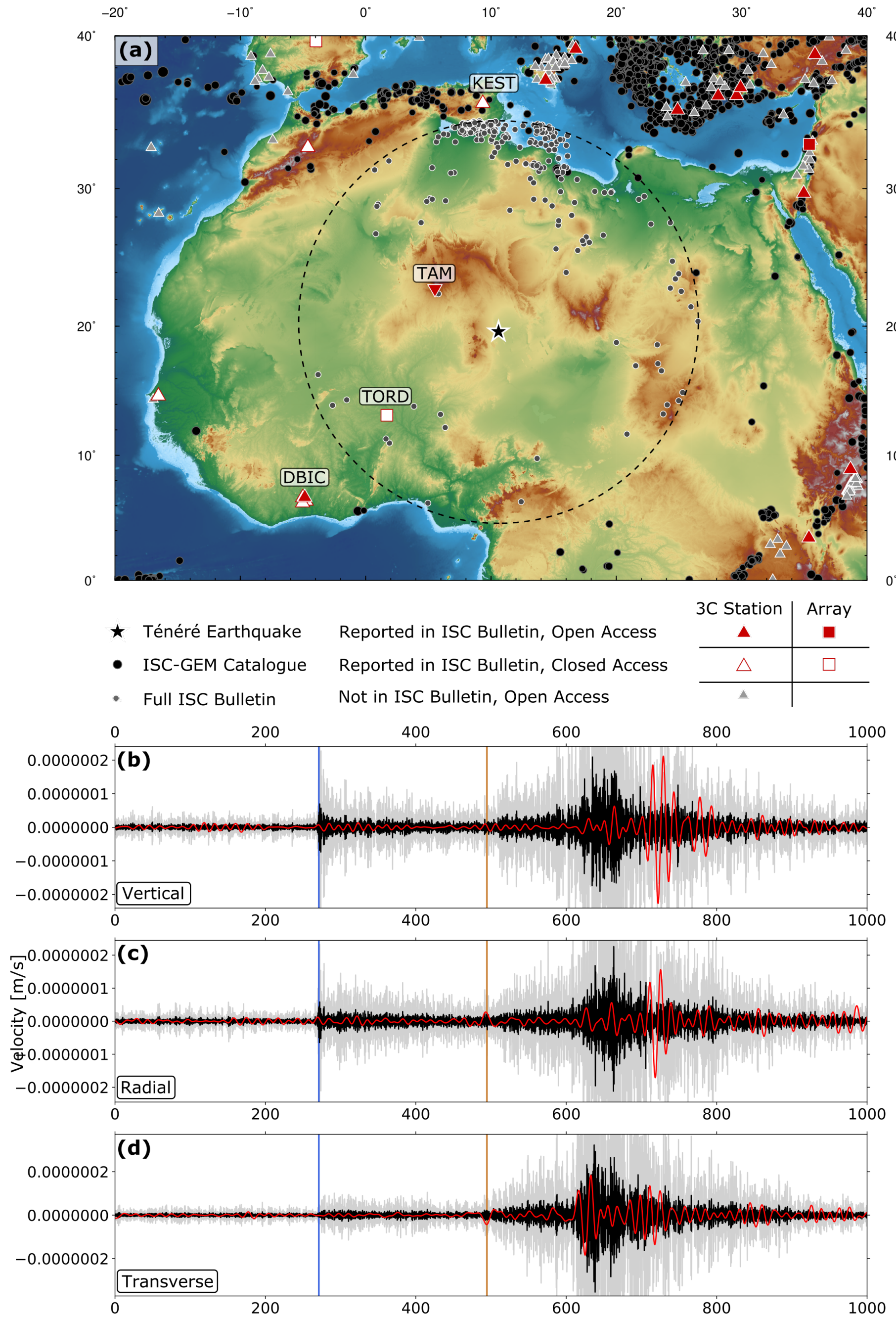

Figure 1: (a) Regional map, showing the 2017 Ténéré earthquake and distribution of observing seismometers. Red filled symbols indicate stations reported in the ISC Bulletin that are Open Access, White-filled symbols are those reported in the ISC Bulletin that are closed, grey are those Open Access 3-component stations not reported in the ISC Bulletin. Inverted red triangle shows the location of the seismometer at Tamanrasset (Algeria), usually reporting to the ISC Bulletin, but inoperative at the time of the 2017 Ténéré earthquake. Black circles show all earthquakes in the ISC-GEM catalogue. Grey circles show every earthquake recorded in the full ISC Bulletin within 15° of the 2017 Ténéré earthquake. (b) Vertical component waveform from DBIC (location shown in (a)). Black trace is filtered between 1.0 and 4.0 Hz, red between 0.02 and 0.08 Hz, to isolate surface wave arrivals, grey is the same as black, with the amplitude scaled by a factor of 5 to emphasise the body wave arrivals. Blue and green bars show the predicted P and S arrival times. (c) as in (b), but showing the radial component waveform. (d) as in (b), but showing the transverse component waveform.

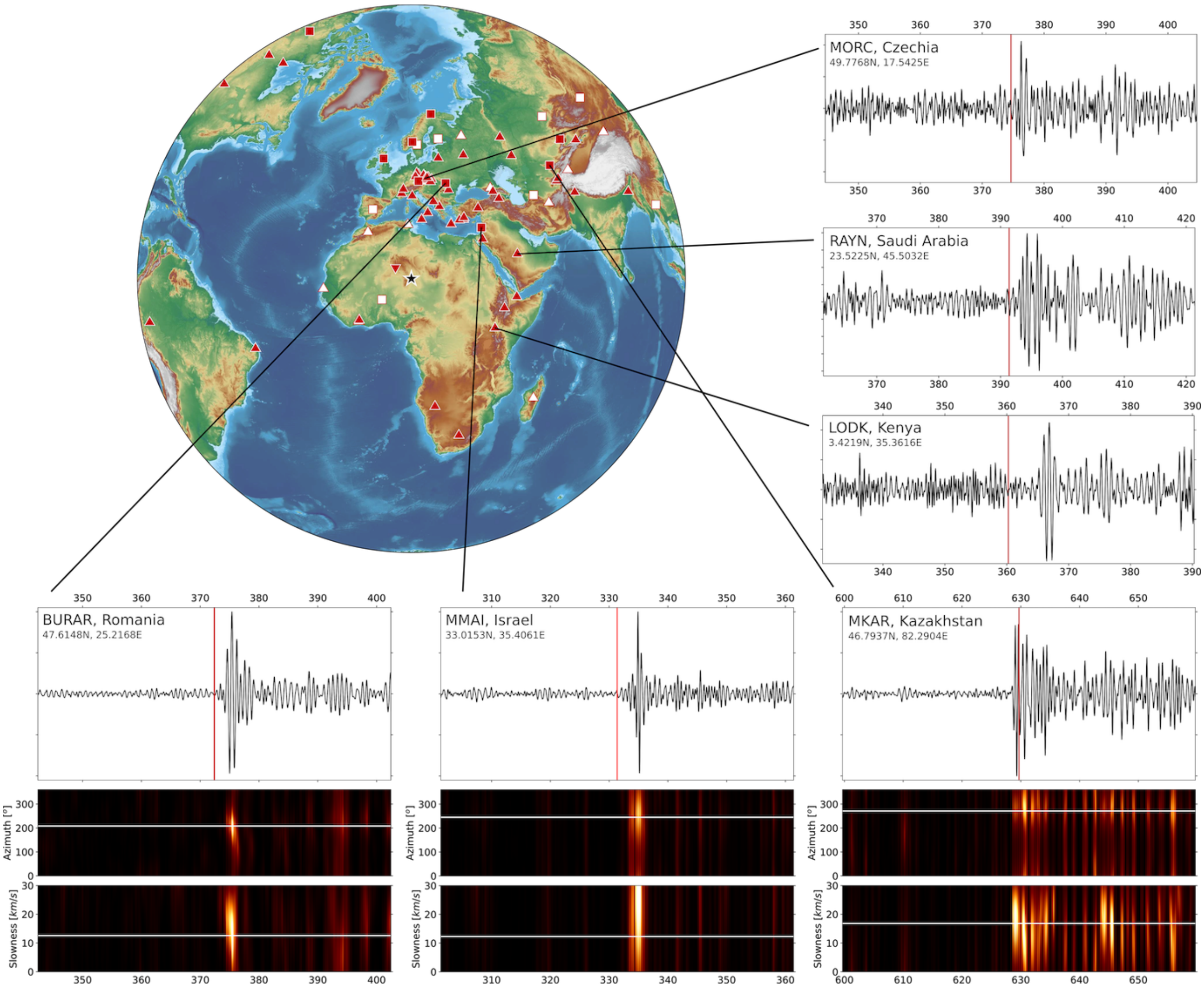

Figure 2: Global station distribution (symbols as in Figure 1). Left panels show 3 vertical component velocity waveforms, filtered between 1 – 3 Hz, from 3-component instruments RAYN, MORC, and LODK. Vertical red line shows the predicted *P*-wave arrival, based on the NEIC location. Lower panels show data from three small-aperture seismic arrays (Bucovina, Mount Meron, and Makanchi), again filtered between 1 – 3 Hz. Top panel shows the beamformed waveform, based on the NEIC location. Lower panels show sweeps through slowness and azimuth space (c.f. Davies et al, 1971), with colour indicating array coherence using the F-statistic (e.g. Blandford, 1974). White lines show the predicted slowness and azimuth for *P*-wave arrivals from the Ténéré earthquake.

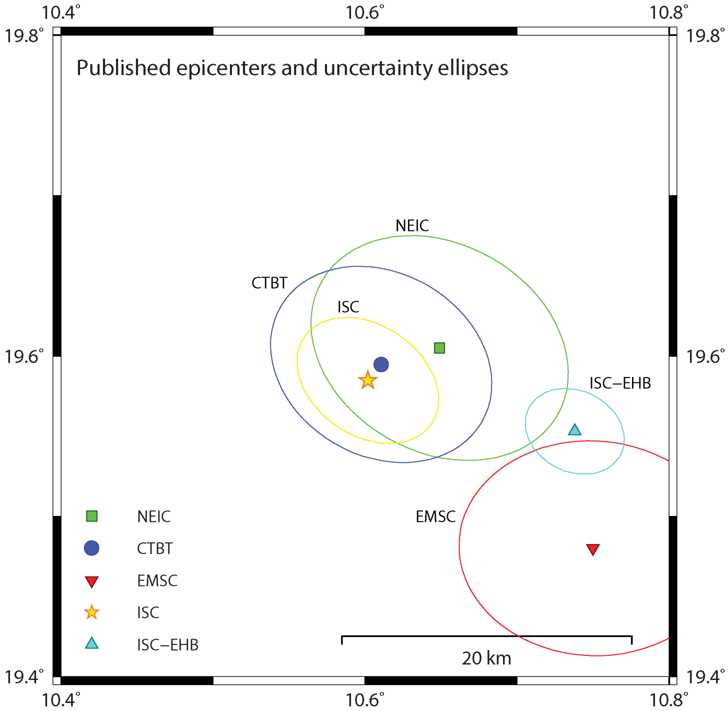

Figure 3: Published location estimates and corresponding 95% confidence ellipses for the January 18, 2017, Niger Earthquake. The epicenters are as provided in Table 1 and the 95% confidence ellipses have (Smaj/Smin/Azimuth) parameters (18.7/14.4/125°) NEIC, (16.0/12.7/120°) CTBT, (18.5/14.9/93°) EMSC, (10.6/7.6/125°) ISC, and (7.1/5.6/117°) ISC-EHB with Smaj and Smin given in km.

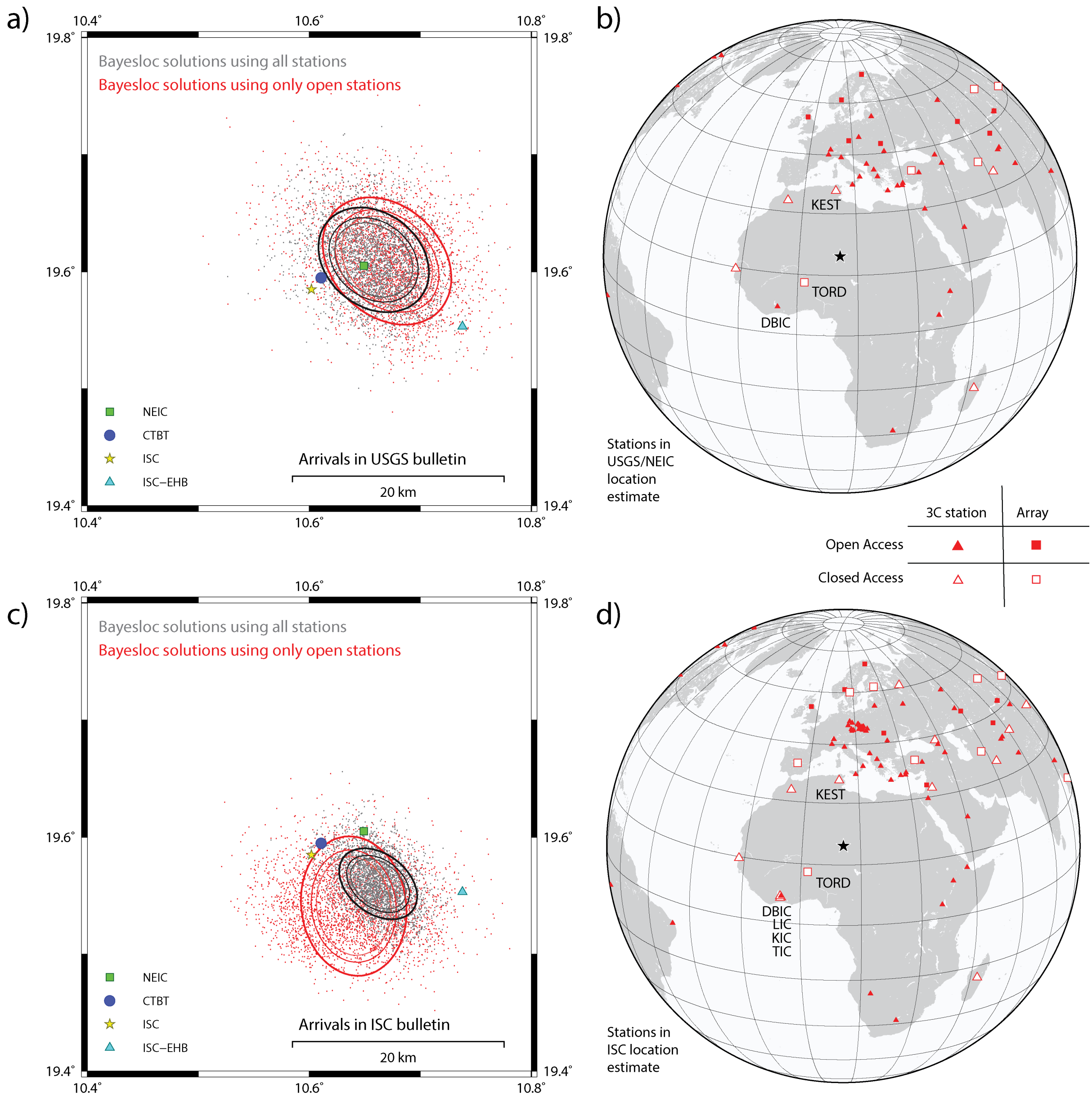

Figure 4: Location estimates obtained using the Bayesloc program with station selections as indicated. Panels (a) and (c) display clouds of the epicenters in the Bayesloc Monte Carlo Markov Chains together with the 90, 95, and 99% confidence ellipses calculated for the scatter plots. Each cloud contains 36000 points. Panels (b) and (d) display the stations used to obtain the solutions displayed in panels (a) and (c) respectively. Key stations are labelled. Stations DBIC, KIC, TIC, and LIC are within tens of kilometers of each other such that they almost appear co-located when displayed on a global scale.

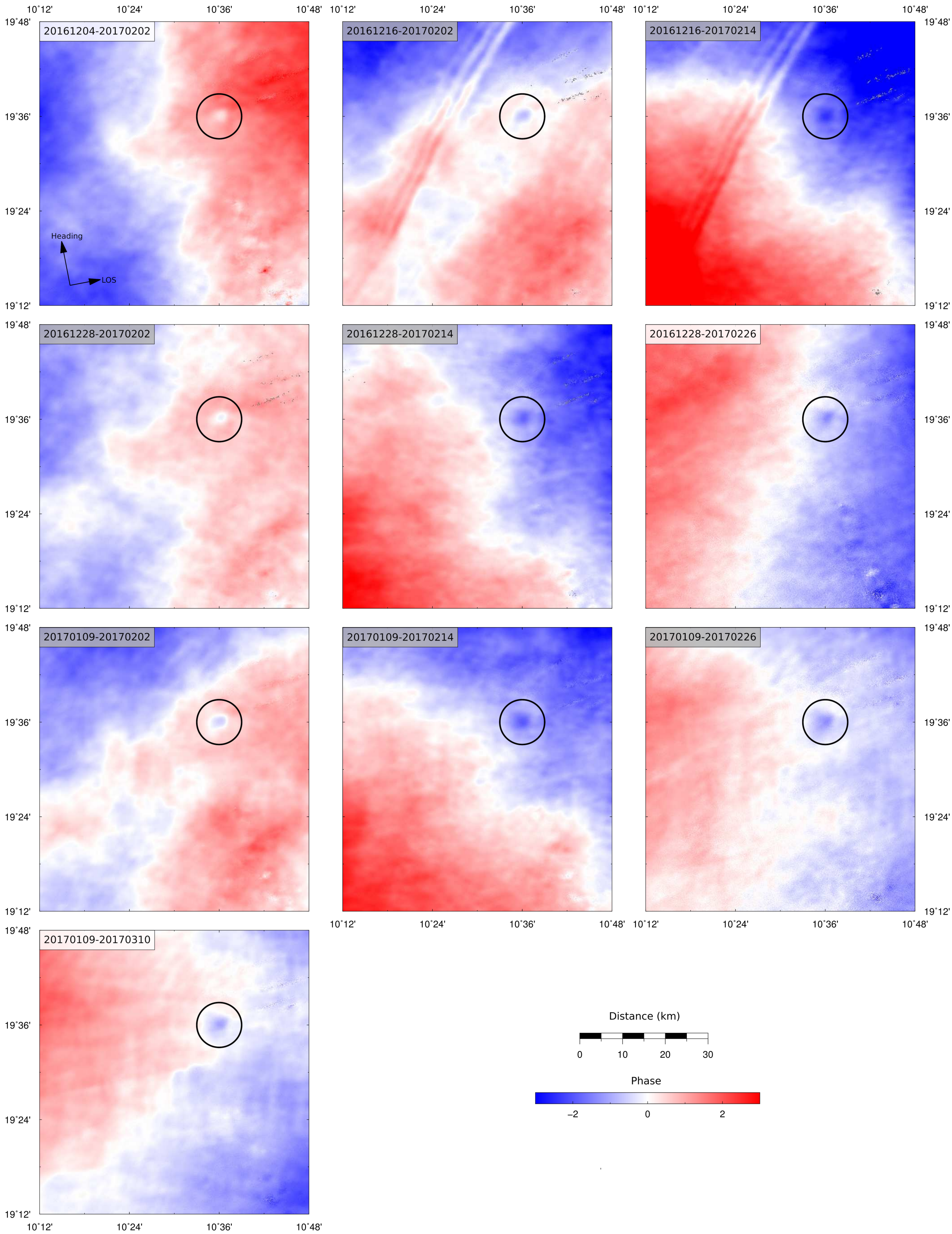

Figure 5: 10 coseismic interferograms, unwrapped. We show equivalent wrapped intereferograms in Figure S1. Colour scale shows multiples of the complete phase cycle. Numeric codes in the top left of each panel indicate the SAR acquisitions used to produce each interferogram. Shading behind numeric codes indicates those independent pairs used in the stack shown in Figure 7. Black circle highlights the consistent signal identified as results from the earthquake. The final panel shows the InSAR coherence for a single interferogram.

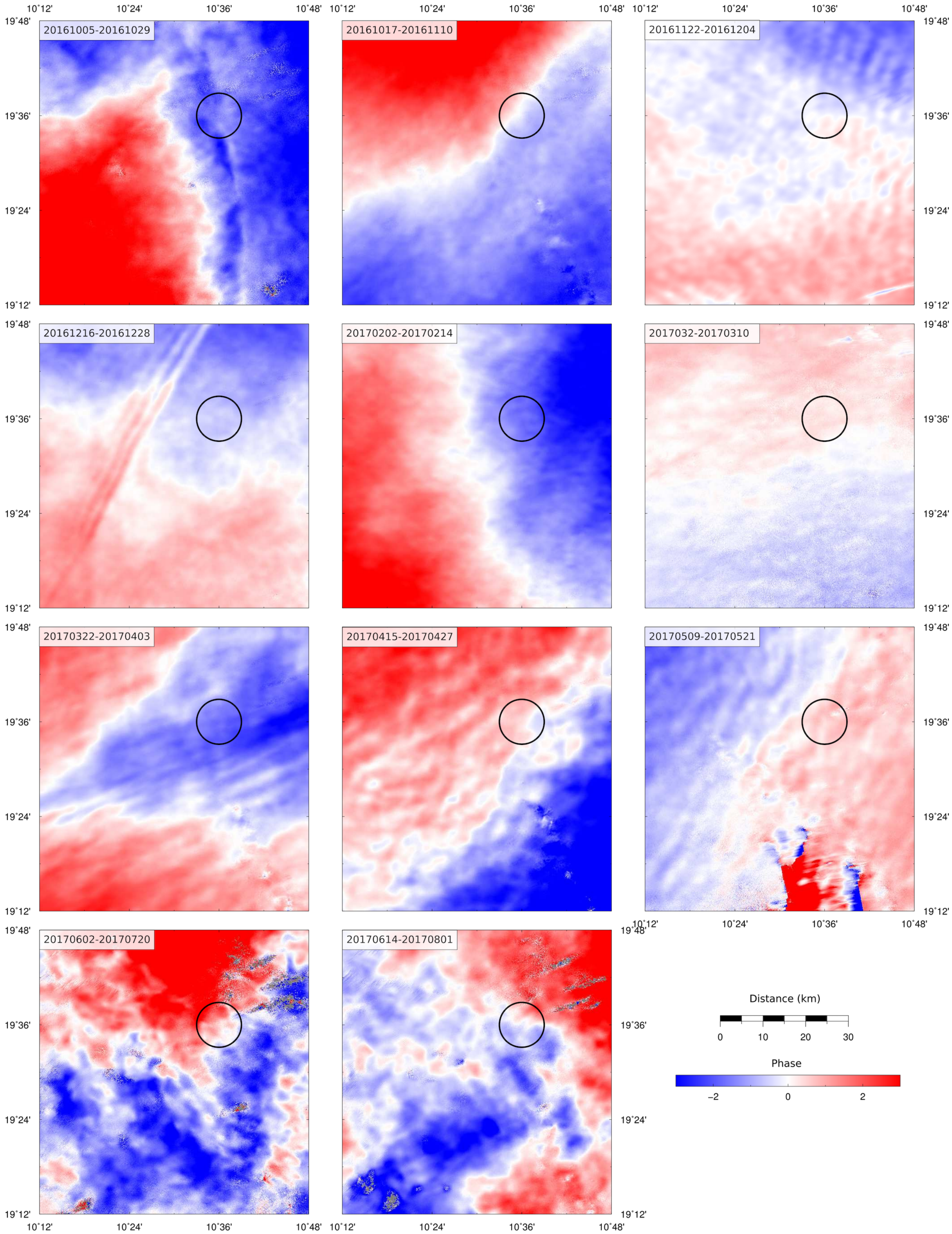

Figure 6: 11 interferograms, unwrapped, that do not span the date of the Ténéré earthquake. Numeric codes in the top left of each panel indicate the SAR acquisitions used to produce each interferogram. Black circle highlights area in which the coseismic interferograms shown in Figure 5 show a consistent deformation signal.

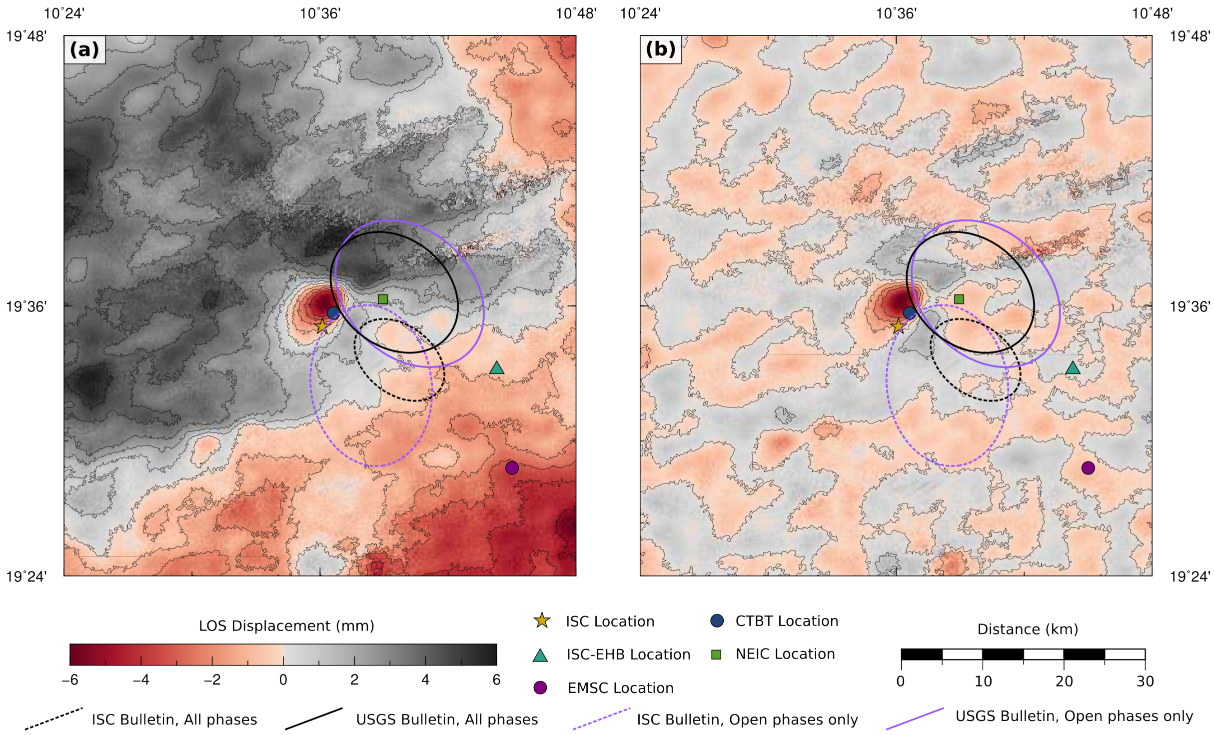

Figure 7: (a) Stacked unwrappped interferogram. (b) Stacked interferogram, filtered between 15 km and 500 m. Colour scale shows line-of-sight displacement. Symbols show seismological locations, as in Figure 3. Contours show 95% interval ellipses determined using different seismic arrival subsets, as described in Figure 4.